A Sub-GHz Multi-ISM-Band ZigBee Receiver Using Function-Reuse and Gain-Boosted N-Path Techniques for IoT Applications

Zhicheng Lin, Pui-In Mak, *Senior Member, IEEE*, and Rui P. Martins, *Fellow, IEEE*

***Abstract*—To address the cost and universality of ultra-low-power (ULP) radios for Internet of Things (IoT) applications, a sub-GHz multi-ISM-band (433/860/915/960 MHz) ZigBee receiver is developed. It features a gain-boosted N-path switched-capacitor (SC) network embedded into a function-reuse RF front-end, offering concurrent RF (common-mode) and BB (differential-mode) amplification, LO-defined RF filtering, and input impedance matching with zero external components. Interestingly, not only the BB power and area are nullified, but also the loading effect between the RF and BB blocks is averted, resulting in better noise figure (NF). Unlike the existing N-path filtering, the described gain-boosted topology offers: 1) double RF filtering at both input and output of the RF front-end; 2) size reduction of the physical capacitors thanks to the Miller multiplication effect, and 3) LO-power saving by decoupling the mixer's on-resistance to the ultimate stopband rejection. Together with a low-voltage LC-VCO with extensively-distributed negative-gain cells for current-reuse with the BB filters, the receiver achieves 8.1 ± 0.6 dB NF, 50 ± 2 dB gain and –20.5 ± 1.5 dBm out-of-band IIP3 at 1.15 ± 0.05 mW power at 0.5 V over the four ISM bands. The active area is 0.2 mm² in 65 nm CMOS.**

***Index Terms*—Blocker NF, CMOS, current reuse, IIP3, Internet of things (IoT), ISM, linear periodically time-variant (LPTV), low-noise amplifier (LNA), mixer, noise figure (NF), out-of-band (OB), phase noise, receiver, ultra-low-power (ULP), ultra-low-voltage (ULV), voltage-control led oscillator (VCO), wireless, ZigBee.**

I. Introduction

With the continued maturation of the Internet of Things (IoT), a huge market has been opening up for short-range ultra-low-power (ULP) wireless connectivity [1], [2]. According to [3], by 2020 the IoT market will be close to hundreds of billion dollars (annually ∼16 billion). To bring down the hardware cost of such massive inter-connections, sub-GHz ULP wireless products compliant with the existing wireless standard such as the IEEE 802.15.4c/d (ZigBee) will be of great demand, especially for those that can cover all regional ISM bands [e.g., China (433 MHz), Europe (860 MHz), North America (915 MHz) and Japan (960 MHz)]. Together with the obvious goals of small chip area, minimum external components and ultra-low-voltage (ULV) supply (for possible energy harvesting), the design of such a receiver poses significant challenges.

The tradeoffs among multi-band operation, power, area and noise figure (NF) are described in Fig. 1. A multi-band receiver [Fig. 1(a)] can be resorted from multiple low-noise amplifier (LNAs) with shared I/Q mixers and baseband (BB) lowpass filters (LPFs). As such, each LNA and its input matching network can be specifically optimized for one band using passive-LC resonators, improving the NF, selectivity and gain. Although a single wideband LNA with zero LC components is preferred to reduce the die size [Fig. 1(b)], the NF and power requirements of the LNA are much higher. Moreover, when the output noise of the LNA is wideband, more harmonic-folding noise will be induced by its subsequent mixers (under hard switching). All these facts render wideband receivers [4] generally more power hungry than its narrowband counterparts [5]–[7].

In contrast, a wide-range-tunable narrowband RF front-end is of greater potential to realize a multi-band ULP receiver. While sub-GHz passive LC resonators are area hungry, the N-path switched-capacitor (SC) network [8], [9] appears as a prospective alternative to replace them. It behaves as a tunable lossy LC resonator with its center frequency accurately defined by the clock. Inspired by it, this paper introduces a function-reuse RF front-end with signal orthogonality [10], and a gain-boosted N-path SC network [11] for tunable RF filtering and input impedance matching. External components are avoided, while multi-band operation, stronger RF filtering, smaller physical capacitor size, and lower LO power are concurrently achieved when compared with the traditional designs [8], [9]. Together with a low-voltage current-reuse VCO-filter, the described multi-band receiver [12] exhibits comparable performances with respect to other single-band-optimized designs [5]–[7], [13]–[16].

Section II overviews the state-of-the-art ULP techniques. The gain-boosted N-path SC network is detailed in Section III,

Manuscript received April 27, 2014; revised August 04, 2014; accepted September 12, 2014. Date of current version November 20, 2014. This paper was approved by Guest Editor Sven Mattisson.

This work was supported by the Macao Science and Technology Development Fund (FDCT) SKL Fund (SKL/AMS-VLSI/MPI) and the University of Macau — MYRG114-FST13-MPI.

Z. Lin and P. Mak are with the State Key Laboratory of Analog and Mixed-Signal VLSI and FST-ECE, University of Macau, Macao, China (e-mail: pimak@umac.mo).

R. P. Martins is with the State Key Laboratory of Analog and Mixed-Signal VLSI and FST-ECE, University of Macau, Macao, China, on leave from the Instituto Superior Técnico, Universidade de Lisboa, Portugal.

Color versions of one or more of the figures in this paper are available online at http://ieeexplore.ieee.org.

Digital Object Identifier 10.1109/JSSC.2014.2358560

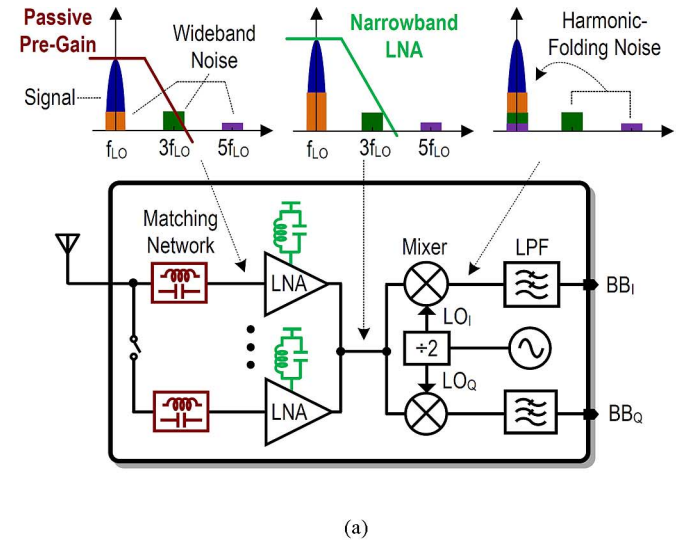

(a)

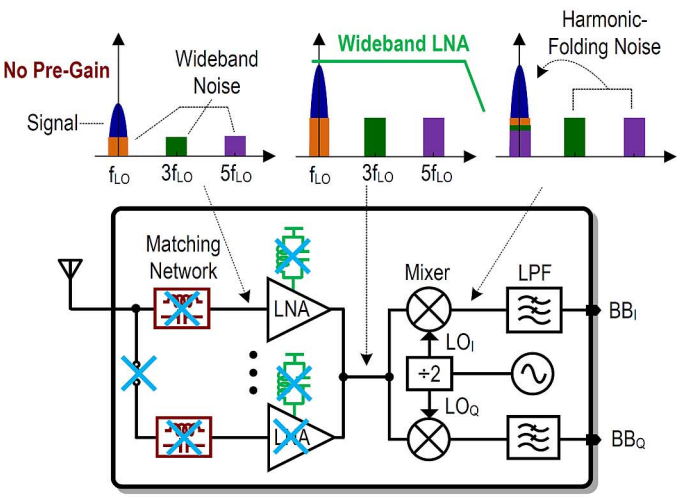

(b)

Fig. 1. Multi-band receiver (a) using multiple LNAs and matching networks for pre-gain and pre-filtering, or (b) using one wideband LNA to save the die area but demanding more power to lower the NF and nonlinearity due to no pre-gain, no pre-filtering and more harmonic-folding noise.

which leads to three receiver architectures having several core properties fundamentally differing from the conventional ones. Section IV details the design of the current-reuse VCO-filter. Measurement results and performance benchmarks are given in Section V, and conclusions are given in Section VI.

II. ULP Techniques: Current Reuse, ULV and Proposed Function Reuse + Gain-Boosted N-Path SC Network

Entered into the nanoscale CMOS regime, the transistors feature sufficiently high f_T and low V_T favoring the use of a current-reuse architecture. Moreover, by conveying the signal in the current domain, both the RF bandwidth and linearity can be improved. Our previous work [15], [16] was inspired by those facts; it unifies most RF-to-BB functions in one cell for current-mode signal processing at a typical 1.2 V supply, resulting in a high IIP3 (-6 dBm) at small power (2.7 mW) and area ($0.3\ mm^2$). Yet, for power savings, another 0.6 V supply

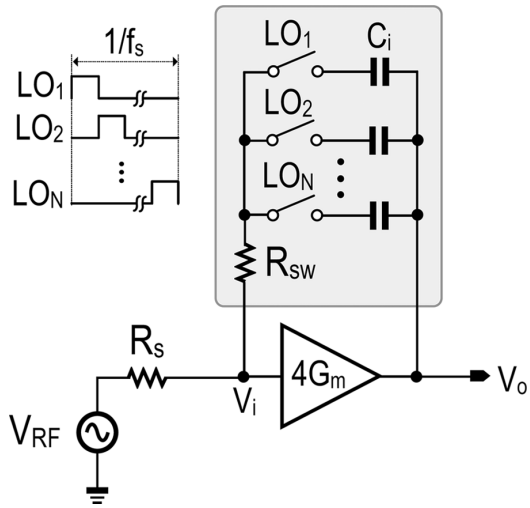

Fig. 2. N-path tunable LNA or bandpass filter [11]. It can provide input impedance matching at V_i.

was still required for the rest of the circuitries, complicating the power management. The 2.4 GHz ULV receiver in [13] and [14] facilitates single 0.3 V operation of the entire receiver at 1.6 mW for energy harvesting, but the limited voltage headroom and transistor f_T call for bulky inductors and transformers to assist the biasing and tune out the parasitics, penalizing the area ($2.5\ mm^2$). Finally, since both of them target only the 2.4 GHz band, a fixed LC network (on-chip in [15], [16] and off-chip in [13], [14]) can be employed for input matching and passive pre-gain (save power). This technique is however costly and inflexible for multi-band designs.

The described multi-band receiver is based on a *function-reuse* RF front-end implemented with a gain-boosted N-path SC network. The cost is low and die area is compact ($0.2\ mm^2$) as on/off-chip inductors and transformers are all avoided except the VCO. The power is squeezed by recycling a set of inverter-based amplifiers for concurrent RF (common mode) and BB (differential mode) amplification, resulting in low-voltage (0.5 V) and low-power (1.15 mW) operation.

III. Gain-Boosted N-Path SC Networks

The proposed gain-boosted N-path SC network can generate an RF output when it is considered as a LNA or bandpass filter [11], or BB outputs when it is considered as a receiver (this work). We describe three alternatives to realize and study such a network. With the linear periodically time-variant (LPTV) analysis, the BB signal transfer function (STF) and noise transfer function (NTF) are derived and analyzed. Besides, three intuitive functional views are given to model their gain responses.

A. N-Path Tunable Receiver

According to [9], by having an N-path SC network as the feedback path of a gain stage (labeled with the symbol $4G_m$), an N-path tunable LNA (or bandpass filter) can be realized with the RF output taken at V_o (Fig. 2). This topology has a number

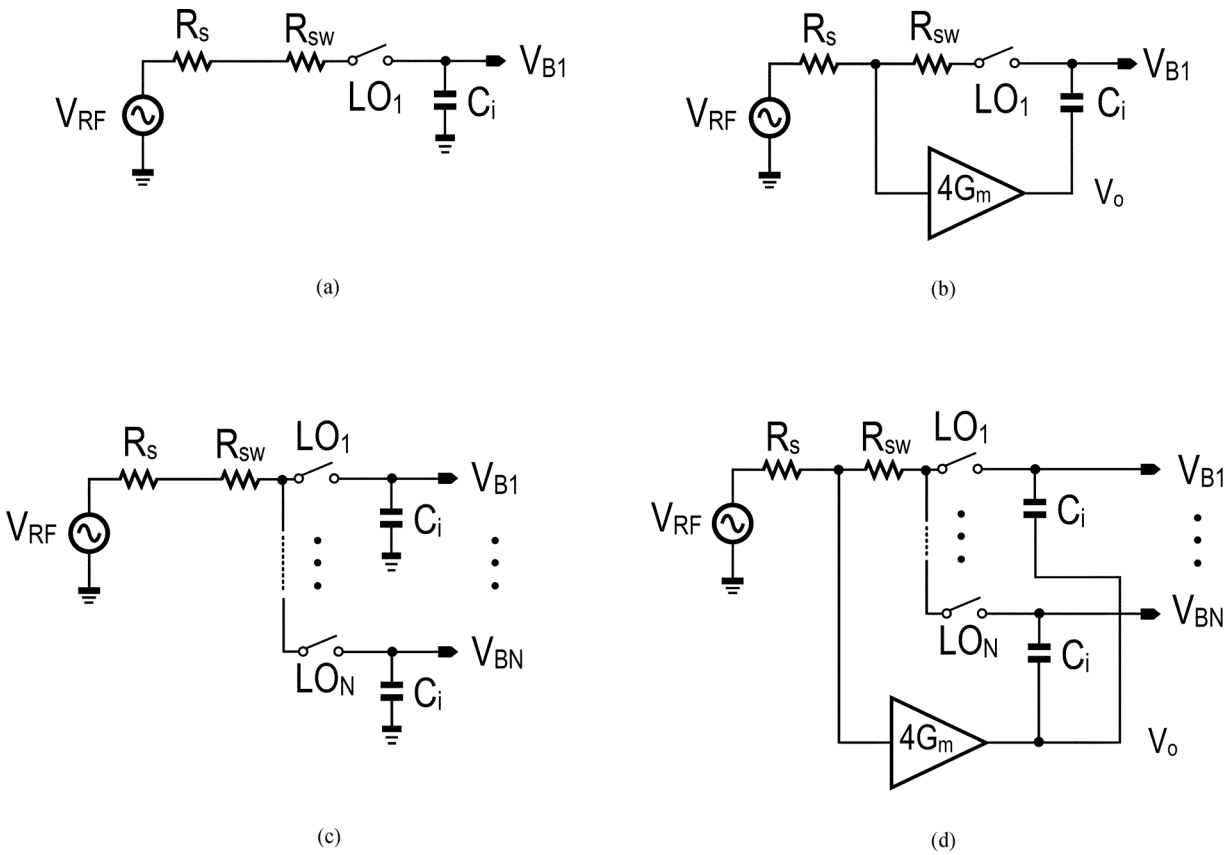

Fig. 3. The N-path tunable LNA in Fig. 2 can be rearranged as an N-path tunable receiver by taking the BB outputs at V_{B1-N} on top of C_i, like a single-path passive mixer with gain boosting as shown in (a)–(b), or an N-path passive mixer with gain boosting as shown in (c)–(d).

of core benefits when compared with the existing N-path filtering [8], [9]. First, double-RF filtering at V_i and V_o is achieved with one N-path SC network. Second, tunable input impedance matching is possible at V_i. Third, the loop gain associated with $4G_m$ reduces the impact of R_{sw} (mixer's ON resistance) to the ultimate out-of-band (OB) rejection. Fourth, similar to the continuous-time Miller capacitor, for a given RF bandwidth (BW), the required C_i can be reduced by the loop gain associated with $4G_m$. Fifth, the NTF of R_{sw} to V_o is a notch function around the clock frequency f_s. Thus, small switches are allowed without degrading the NF, saving the LO power. Finally, the output noise at V_o is narrowband with a comb-filter shape, reducing the harmonic-folding noise when it is followed by a wideband passive mixer.

Interestingly, if such an operation principle is extended to Fig. 3(a)–(d), the N-path tunable LNA can be viewed as a passive-mixer receiver, with all capacitors C_i driven by a $4G_m$ stage. The BB outputs are taken at V_{B1-N}. Unlike the original passive-mixer-first receiver [17], [18] that offers no gain at V_{B1-N}, this receiver has a relatively large BB gain at V_{B1-N} surmounting the NF limitation. The frequency-translational RF filtering at V_i and V_o are realized by LO_1–LO_N to upconvert the BB signals V_{B1-N} to RF, and in-phase summed together.

To establish a basic operation theory, the analysis below follows the LPTV method [11], [19]. For simplicity, $N = 4$ is employed to allow basic I/Q downconversion with LO_1–LO_4 as 25%-duty-cycle non-overlapping clocks. The timing diagram of LO_1 is shown in Fig. 4(a). $4G_m$ can be based on a self-biased inverter amplifier with g_{m1} as the transconductance, R_L as the output resistance and R_{F1} as the feedback resistor. LO_{2-4} are similar to LO_1 with a time delay. The analysis is conducted for V_{B1} while for V_{B2-4}, when f_{RF} is around qf_s, the phase relation between the BB voltages V_{Bi} $(1 \le i \le 4)$ can be described by $V_{Bm} = V_{Bn}e^{jq\pi(m-n)/2}$, $(1 \le (m,n) \le 4)$. Thus, V_{B1} and V_{B3} (V_{B2} and V_{B4}) are either out-of-phase or in-phase with each other, depending on the input frequency. When LO_1 is high $(K = 1)$, linear analysis reveals the following state-space description:

$$\frac{dv_{Ci}(t)}{dt} = \frac{v_{RF}(t)}{C_i R_1} - \frac{v_{Ci}(t)}{C_i R_2} \tag{1}$$

where

$$R_1 = \frac{1 + \frac{R_{sw}}{R_{F1}} + \frac{R_{sw}+R_s}{R_L} + \frac{R_{sw}R_s}{R_{F1}R_L} + g_{m1}R_S + \frac{g_{m1}R_{sw}R_S}{R_{F1}}}{\frac{1}{R_L} + g_{m1}} \tag{2}$$

$$R_2 = \frac{1 + \frac{R_{sw}}{R_{F1}} + \frac{R_{sw}+R_s}{R_L} + \frac{R_{sw}R_s}{R_{F1}R_L} + g_{m1}R_S + \frac{g_{m1}R_{sw}R_S}{R_{F1}}}{\frac{1}{R_{F1}} + \frac{1}{R_L} + \frac{R_S}{R_{F1}R_L} + \frac{g_{m1}R_S}{R_{F1}}}. \tag{3}$$

When LO_1 is low $(K = 2)$, we have

$$\frac{dv_{Ci}(t)}{dt} = 0. \tag{4}$$

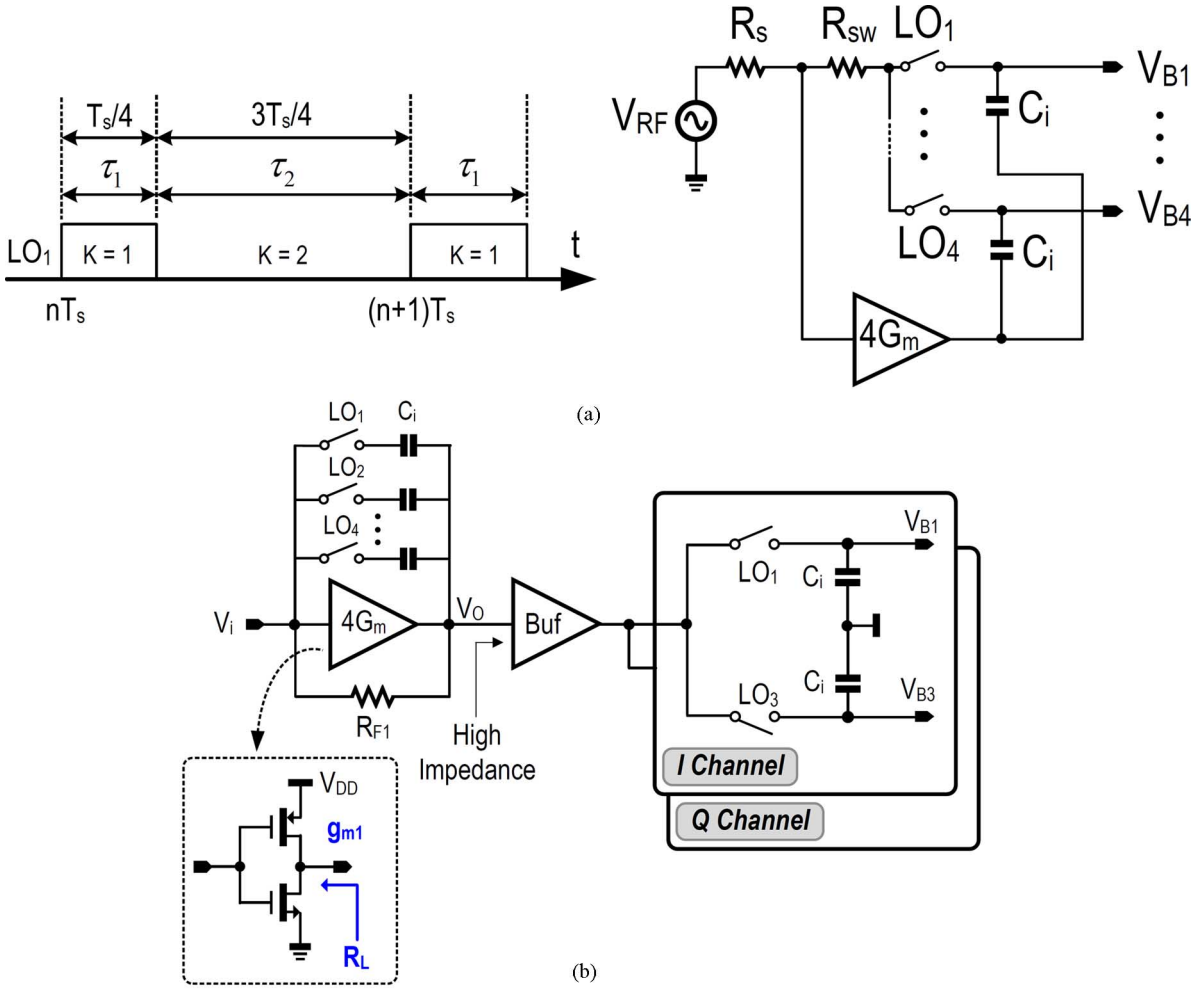

Fig. 4. (a) Timing diagram of LO_1 and the 4-path tunable receiver. (b) Functional view of a 4-path tunable receiver to model the gain response.

From (1)–(4), the harmonic transfer functions (HTFs) for the intervals $\mathrm{K}=1$ and $\mathrm{K}=2$ are derived in (5) and (6), respectively:

$$\mathrm{H_{n,1,RF}(j\omega)}=\frac{\omega_{\mathrm{rc,B}}}{\omega_{\mathrm{rc,A}}+\mathrm{j}\omega}\times\frac{1-\mathrm{e}^{-\mathrm{jn}\omega_\mathrm{s}\tau_1}}{\mathrm{j}2\pi\mathrm{n}}+\frac{1-\mathrm{e}^{\mathrm{j}\omega\tau_2}}{\omega_{\mathrm{rc,A}}+\mathrm{j}\omega}\mathrm{G(j}\omega\mathrm{)f_s} \tag{5}$$

$$\mathrm{H_{n,2,RF}(j\omega)}=-\frac{1-\mathrm{e}^{\mathrm{j}\omega\tau_2}}{\mathrm{j}\omega}\mathrm{G(j}\omega\mathrm{)f_s} \tag{6}$$

where

$$\mathrm{G(j\omega)}=\frac{\mathrm{e}^{\mathrm{j}(\omega-\mathrm{n}\omega_\mathrm{s})\tau_1}\mathrm{e}^{-\omega_{\mathrm{rc,A}}\tau_1}}{\mathrm{e}^{\mathrm{j}2\pi(\omega-\mathrm{n}\omega_\mathrm{s})/\omega_\mathrm{s}}-\mathrm{e}^{-\omega_{\mathrm{rc,A}}\tau_1}}\times\frac{1}{\frac{\omega_{\mathrm{rc,A}}}{\omega_{\mathrm{rc,B}}}+\frac{\mathrm{j}(\omega-\mathrm{n}\omega_\mathrm{s})}{\omega_{\mathrm{rc,B}}}}, \tag{7}$$

$\omega_{\mathrm{rc,A}}=1/\mathrm{R_2C_i}$, $\omega_{\mathrm{rc,B}}=1/\mathrm{R_1C_i}$, $\tau_1=\mathrm{T_s}/4$ and $\tau_2=3\mathrm{T_s}/4$. Here, $\mathrm{G(j}\omega\mathrm{)}$ represents the switching moment transfer function as defined and calculated in [11], [19]. By combining (5)–(7), the harmonics transfer function from $\mathrm{V_{RF}}$ to $\mathrm{C_i}$ is derived:

$$\mathrm{H_{n,RF}(j\omega)}=\frac{\mathrm{V_{Ci}(j\omega)}}{\mathrm{V_{RF}(j\omega)}}=\mathrm{H_{n,1,RF}(j\omega)}+\mathrm{H_{n,2,RF}(j\omega)}. \tag{8}$$

For the BB signal around $\mathrm{f_s}$, the voltages sampling at $\mathrm{C_i}$ are differential, and $\mathrm{V_o}$ is thus the virtual ground and the state of the circuit $\mathrm{V_{Ci}(j\omega)}$ (voltage across $\mathrm{C_i}$) is equal to $\mathrm{V_{Bm}(j\omega)}$, where $1\le\mathrm{m}\le4$. Although the results from the LPTV analysis are exact, they are lacking in conceptual intuition that can be of more practical value for designers. To compare with the usual receiver concept that is based on cascade of blocks, a functional view of a 4-path tunable receiver is given in Fig. 4(b) to model the gain response. An ideal buffer amplifier (infinite input impedance and zero output impedance) is introduced into the model implying that the passive mixer has no loading effect to the front-end $4\mathrm{G_m}$ stage. Note that the model is inapplicable for studying the noise, since the noise sources from the functional view are separated, and thus considered as uncorrelated. Differently with the noise sources of the proposed receiver, they are considered as correlated. From this functional view, the mixers are reused for two roles: double-RF filtering (i.e., as two N-path filters at both input and output of the gain stage) and frequency downconversion (i.e., as an N-path mixer). For the associated capacitors, they are also reused for both double-RF filtering (associated with the 4-path SC network) and BB filtering at $\mathrm{V_{B1-4}}$. These properties lower the LO power and chip area while providing stronger RF filtering. For the RF gain at

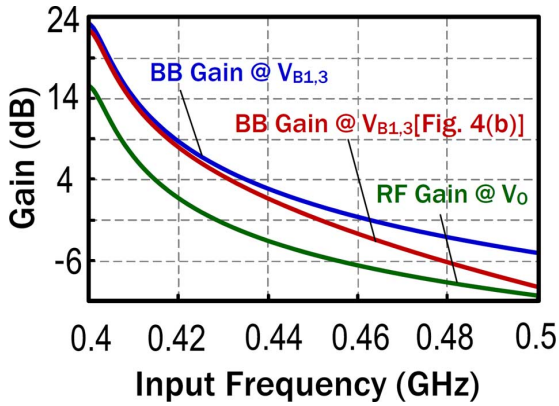

Fig. 5. Simulated BB gain and RF gain of the 4-path tunable receiver (Fig. 4(a)), and the simulated BB gain from the functional view in Fig. 4(b).

$V_{o'}$, although it has been studied in [11] by the LPTV analysis, it can also be derived by the upconversion of V_{B1-4} and summed together at V_o as given by

$$v_o(t) = \sum_{m=1}^{4} v_{Bm}(t) LO_m(t). \tag{9}$$

After applying Fourier series analysis to (9) around f_s, we have

$$V_o(j\omega)\frac{2\sqrt{2}}{\pi}V_{B1}(j\omega) = \frac{\sqrt{2}}{\pi}V_{B1,3}(j\omega) \tag{10}$$

which is an approximation as the influence of R_{sw} is ignored. Here $V_{B1,3} = V_{B1} - V_{B3}$. To verify it, the BB and RF STFs of the N-path tunable receiver are plotted together in Fig. 5. The RF gain is $\sim$ 8 dB smaller than that of the BB gain, close to the prediction by (10). Also, the BB gain from the functional view is plotted, which fits well with the original gain-boosted in-band (IB) signal.

The power spectral density (PSD) of the BB output noise is derived in Appendix A, while the PSD of the RF output noise at V_o has been studied in [11]. The simulated results are given in Fig. 6 (using the model of Fig. 17 in Appendix A). From simulations, the differential output noise power from R_{sw} and R_{F1} are much smaller (around two orders of magnitude) than that from R_s and $4G_m$. Thus, the noise contributions from R_{sw} and R_{F1} are greatly suppressed, making small mixer's switches and large R_{F1} possible (constrained by input impedance matching and the required RF filtering). Unlike the passive-mixer-first receiver [17], [18] where the BB NF from R_{sw} is approximately $(R_{sw}/R_s + \gamma)$, here γ is a factor from the harmonic folding. Thus, for the passive-mixer-first design, the BB NF due to R_{sw} is usually of a similar order of magnitude as R_s. Besides, a small R_{sw} and additional LO paths are required to minimize such effect.

We also show the simulated BB NF for $V_{B1,3}$ and RF NF at V_o (Fig. 7), where $V_{B1,3} = V_{B1} - V_{B3}$ and similar notations such as $V_{X1,3} = V_{X1} - V_{X3}$ have the same implication in the following text. Interestingly, the BB NF is smaller than the RF NF at the LNA's output V_o, since the BB gain (or noise) and RF gain (or noise) are concurrent but happened under different STF (or NTFs). This characteristic underlines a fundamentally different concept when compared with the traditional receiver that is based on the cascade of blocks, where the RF NF should be smaller than the BB NF. Note that for the BB NF, the even-harmonic-folding noise due to the LO contributes only common-mode noise at the BB outputs, which will be rejected differentially. However, it will contribute to the RF noise at V_o due to its single-ended nature. This is one of the senses that the BB NF can be smaller than the RF NF. The authors are still pursuing deeper exploration of this topic and this paper serves as the foundation. Furthermore, the $1/f$ noise around DC from the transconductance devices are upconverted to f_s with little influence to the total output noise at DC [as shown in (A1)]. This was verified by simulations (Fig. 7) where the BB NF at 1 kHz has increased by only 0.15 dB. Thus, short channel-length devices can be employed without degrading the BB low-frequency noise.

B. AC-Coupled N-Path Tunable Receiver

Another alternative to implement such a gain-boosted N-path SC network is shown in Fig. 8(a). The mixers are placed on the feedback path while the input is AC-coupled by capacitors that simplify the cascading of itself for a higher order of filtering. Without considering the memory effect of capacitor C_i, the operation of this architecture can be explained as follows: Initially, at RF frequency, the capacitor C_i can be assumed as a short circuit. The input signal V_{RF} is thus directly coupled to each gain stage G_m (G_m has a transconductance of g_{m2}, output resistance of $4R_L$, and feedback resistor of R_{F2}) and is amplified along path A [Fig. 8(a)] while the signal along the feedback path is downconverted to BB and summed at V_o, which will be zero since LO_1 and LO_3 are 180° out-of-phase with each other (the same is true for $LO_{2,4}$). After that, the amplified RF signal at V_o is immediately down-converted to BB by the 4-path I/Q passive mixers along path B [Fig. 8(b)]. The BB signals at $V_{B1,I+}$ and $V_{B1,I-}$ are differential (the same is true for $V_{B1,Q+}$ and $V_{B1,Q-}$). Thus, node V_i is a virtual ground. The I/Q BB signals will be amplified and summed together again at V_o, which should be zero. This process is explicitly modeled in Fig. 8(c). Similar to Fig. 4(b), an ideal buffer amplifier is inserted between the front-end gain stage (with small signal transconductance g_{m1} and feedback resistor $R_{F2}/4$ for the $4G_m$ stage, as the 4 paths are parallelized) and I/Q passive mixers. When the memory effect of C_i is accounted, the 4-path SC network can be modeled at the feedback path of the $4G_m$ stage, providing double-RF filtering at both its input and output nodes.

With sufficiently large R_{F2}, the voltages (i.e., the circuit states) sampling at C_i are independent [19]. Around the clock frequency, in the steady state, the BB voltages sampling at C_i are $v_{Ci}(t)$, $jv_{Ci}(t)$, $-v_{Ci}(t)$ and $jv_{Ci}(t)$ respectively for

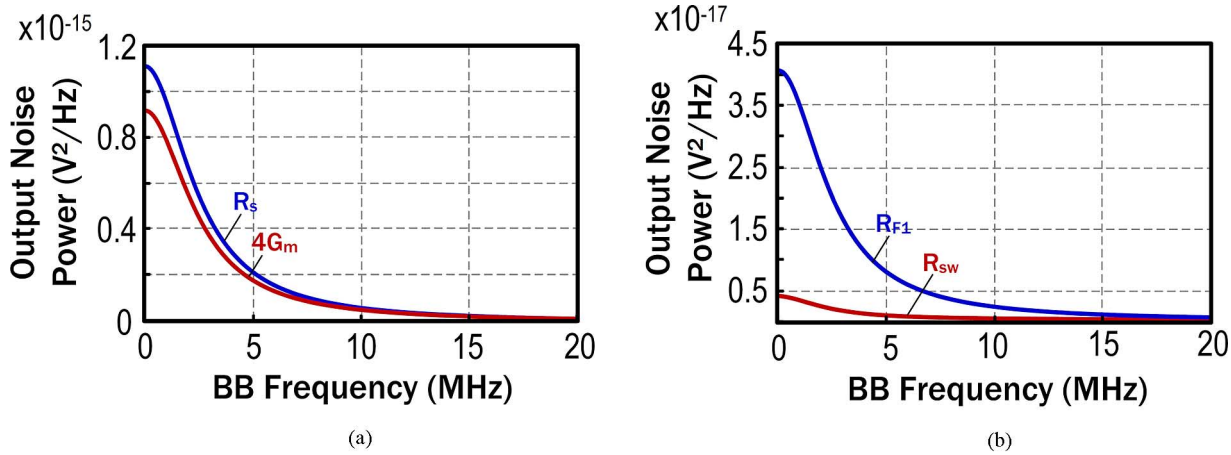

(a) (b)

Fig. 6. (a) Simulated output-noise PSD at the differential BB outputs ($V_{B1,3}$) due to (a) R_s and $4G_m$. (b)R_{sw} and R_{F1}. The simulation parameters are $R_L = 800\ \Omega$, $R_s = 50\ \Omega$, $R_{sw} = 30\ \Omega$, $g_{m1} = 20.55$ mS, $C_i = 12.5$ pF, $f_s = 400$ MHz, $R_{F1} = 5$ kΩ, $\overline{V^2_{n,sw}} = 4kTR_{sw} = 4.968 \times 10^{-19}(V^2/Hz)$, $\overline{V^2_{n,Rs}} = 4kTR_s = 8.28 \times 10^{-19}(V^2/Hz)$, $\overline{V^2_{n,4gm1}} = 4kT/g_{m1} = 8.058 \times 10^{-19}(V^2/Hz)$ and $\overline{V^2_{n,RF1}} = 4kTR_{F1} = 828 \times 10^{-19}(V^2/Hz)$.

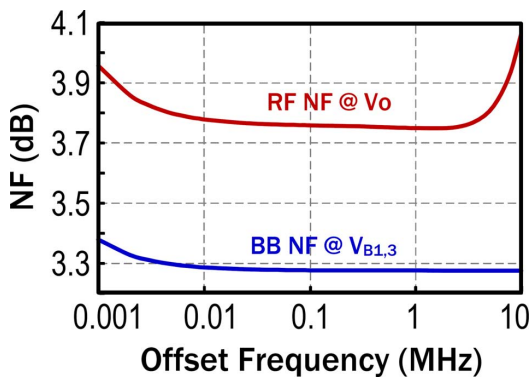

Fig. 7. Simulated NF of the N-path tunable receiver with the RF output (RF NF @ V_o) or BB outputs (BB NF @ $V_{B1,3}$).

LO_{1-4}. When LO_1 is high, linear analysis shows the following state-space description:

$$\begin{cases} \frac{C_i dv_{Ci}(t)}{dt} = \frac{v_o(t)}{R_L} + (v_{B1,I+}(t) + v_{B1,I-}(t) + v_{B1,Q+}(t) \\ \qquad +v_{B1,Q-}(t))g_{m2} \\ \frac{v_{RF}(t)-v_i(t)}{R_S} = \frac{C_i dv_{Ci}(t)}{dt} \\ v_i(t) = v_{Ci}(t) + v_o(t) + R_{sw}\frac{C_i dv_{Ci}(t)}{dt} \\ v_i(t) - v_{B1,I+}(t) = v_{Ci}(t) \\ v_i(t) - v_{B1,I-}(t) = -v_{Ci}(t) \\ v_i(t) - v_{B1,Q+}(t) = jv_{Ci}(t) \\ v_i(t) - v_{B1,Q-}(t) = -jv_{Ci}(t). \end{cases} \tag{11}$$

Simplifying (11), the same equation as in (1) is obtained, with $R_{F1} = \infty$ for R_1 and R_2. When LO_1 is low, it is in the hold mode, which can be described by (4). Thus, the same BB voltages $V_{B1,I\pm}(V_{B1,Q\pm})$ as in GB-SC are expected. For the RF voltage at V_o, it can be evaluated by (10), rendering the same RF voltage gain as in Fig. 2. For the BB NTF from G_m, R_{sw}, R_s and R_{F2}, they are also similar to those of Fig. 2 (not shown here).

If R_{F2} is small, the voltage sampling at C_i during each LO cycle will be leaked to the ground through R_{F2}, or coupled with other states at the output V_o. The effect of charge leakage or sharing will decrease both the BB and RF gains. In the proposed gain-boosted SC network, however, there is no such a problem since the charge stored at the capacitors is constant. Thus, this architecture has smaller gain than the gain-boosted N-path SC network under a finite feedback resistor with all other parameters unchanged. In a similar way, the AC-coupled N-path tunable receiver blocks the DC response, since at DC the charge stored at the capacitors C_i has infinite time to disappear.

C. Function-Reuse Receiver Embedding a Gain-Boosted N-Path SC Network

Unlike the AC-coupled N-path tunable LNA, the proposed function-reuse receiver with a gain-boosted 4-path SC network [Fig. 9(a)] separates the output of each gain stage G_m (G_m has a transconductance of g_{m3}, output resistance of $4R_L$, and feedback resistor of R_{F3}) with capacitor C_o that is an open circuit at BB. The I/Q BB signals at $V_{B1,I\pm}$ and $V_{B1,Q\pm}$ are further amplified along the Path C [Fig. 9(b)] by each G_m stage. With the memory effect of the capacitors, the functional view of the gain response is shown in Fig. 9(c). In order to achieve current-reuse between the RF LNA and BB amplifiers without increasing the supply, the circuit published in [10] with an active mixer has a similar function. However, the BB NF behavior and the RF filtering behavior are different from the N-path passive mixer applied here that is at the feedback path. For the BB amplifiers, it is one G_m with one R_{F3}, balancing the BB gain and OB-IIP3. After considering that the BB amplifiers have been absorbed in the LNA, the I/Q passive mixers and capacitors absorbed by the 4-path SC network, the blocks after the LNA can be assumed virtual. These virtual blocks reduce the power, area and NF. Similar to the AC-coupled N-path tunable LNA, with a relative small R_{F3}, the voltage sampling at C_i in different phases will either leak to the ground, or couple with each other, lowering the BB and RF gains.

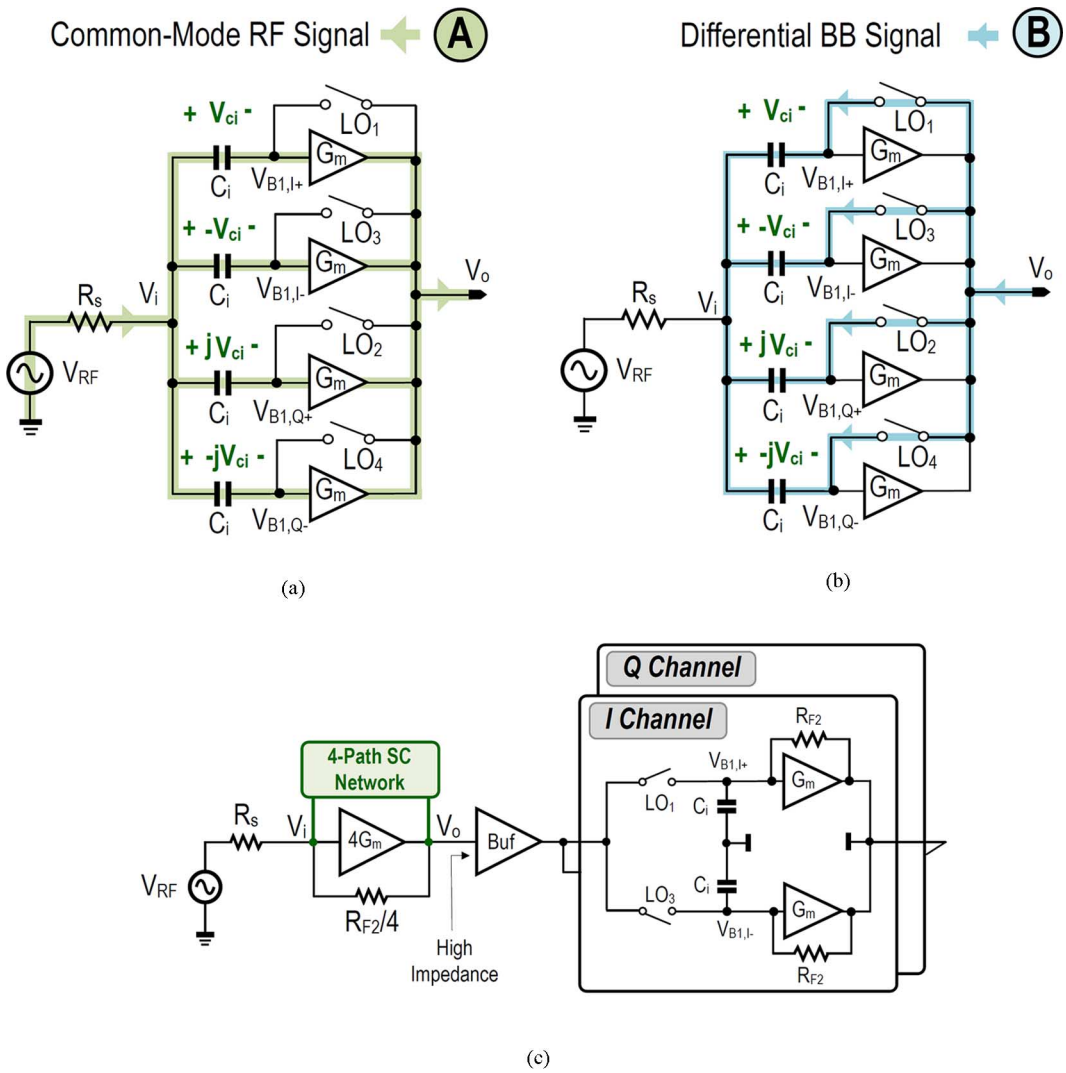

Fig. 8. (a) AC-coupled 4-path tunable receiver and its operation for RF signal, (b) BB signals and (c) its functional view to model the gain response.

To validate the above analysis, the gain and noise performances under two sets of R_{F3} are simulated. Here, the virtual blocks in Fig. 9(c) are implemented with physical transistors and capacitors for the BB amplifiers and the mixers while the buffer is ideal. Thus, the power of the modeled receiver is at least 2× larger than the proposed receiver. For the IB BB gain at $V_{B2,I\pm}(V_{B2,Q\pm})$ between the proposed function-reuse receiver and its functional view, the difference is only 1 dB at a large R_{F3} of 150 kΩ [Fig. 10(a)]. For a small R_{F3}, the gain error goes up to 2 dB [Fig. 10(b)], which is due to the gain difference between the model of the N-path tunable LNA [Fig. 9(c)] and the implementation of the function-reuse receiver that has AC-coupling. For the NF difference (ΔNF), with a large (small) R_{F3}, it is ∼ 0.8 dB (3.5 dB) as compared in Fig. 11(a) and (b). This is due to the lower gain at the LNA's output, forcing the input-referred noise from the downconversion passive mixers and the BB amplifiers to increase with a small R_{F3}. Either with a small or large R_{F3}, it is noteworthy that the variation of BB NF is small (i.e., for $R_{F3} = 20$ kΩ it is 3.6 dB while for $R_{F3} = 150$ kΩ it is 3.4 dB), because the BB NTF has a weak relation with R_{F3}. It also indicates that the BB NTF is weakly related with the gain at the LNA's output, which is dissimilar to the usual receiver where the NF should be small when the LNA's gain is large. Similarly, the NF at the LNA's output (now shown) can be larger than that at BB due to the different NTFs. The BB gain and the output noise at $V_{B2,I\pm}(V_{B2,Q\pm})$ are further discussed in Appendix B.

For the RF gain at $V_\circ$, the simulations results are shown in Fig. 12(a) for the three realizations. With relatively small feedback resistors $R_{F1} = 5$ kΩ, $R_{F2} = R_{F3} = 20$ kΩ, the function-reuse receiver has about 10 dB smaller IB gain than the other two. Also, there is a gain response appearing at the 2^{nd} harmonic, which is due to the single-ended realization. The IB gain loss of the function-reuse receiver can be compensated by increasing R_{F3} from 20 to 150 kΩ, with all other parameters unchanged. The corresponding RF gain responses are plotted in Fig. 12(b). All results are consistent to each other (and this is also true for the BB gain). The NFs at the LNA's output $V_\circ$ are plotted in Fig. 12(c). With a small R_{F1-3}, the RF NF of the function-reuse receiver is higher due to a lower IB gain [the RF NF is also much higher than the BB NF, as shown in Fig. 11(b)]. How-

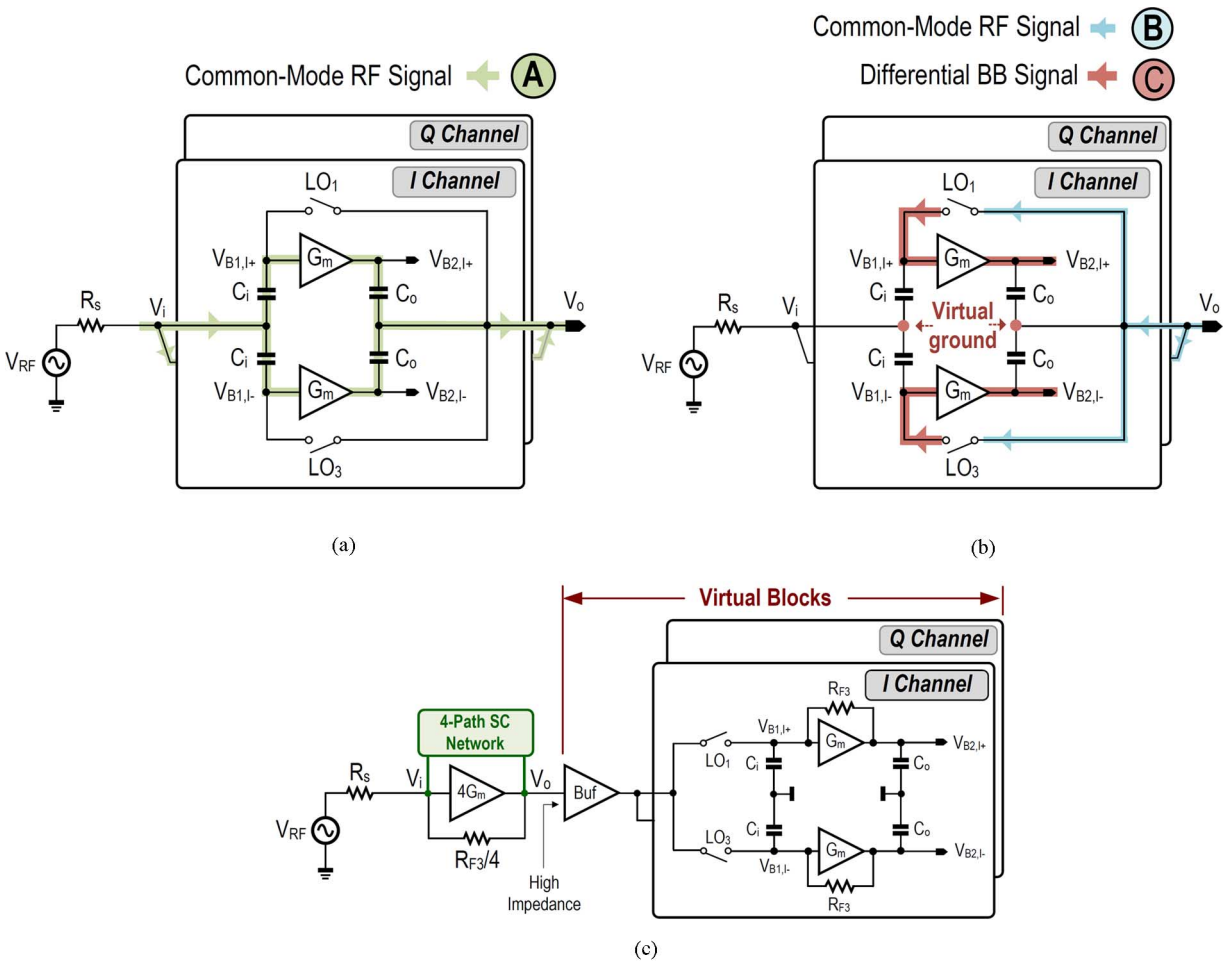

Fig. 9. (a) Function-reuse receiver embedding a gain-boosted 4-path SC network and its operation for RF signal, (b) BB signals and (c) its functional view to model the gain response. For simplicity, the front-end gain stage $4G_m$ and its 4-path SC network follow the structure of Fig. 4(b).

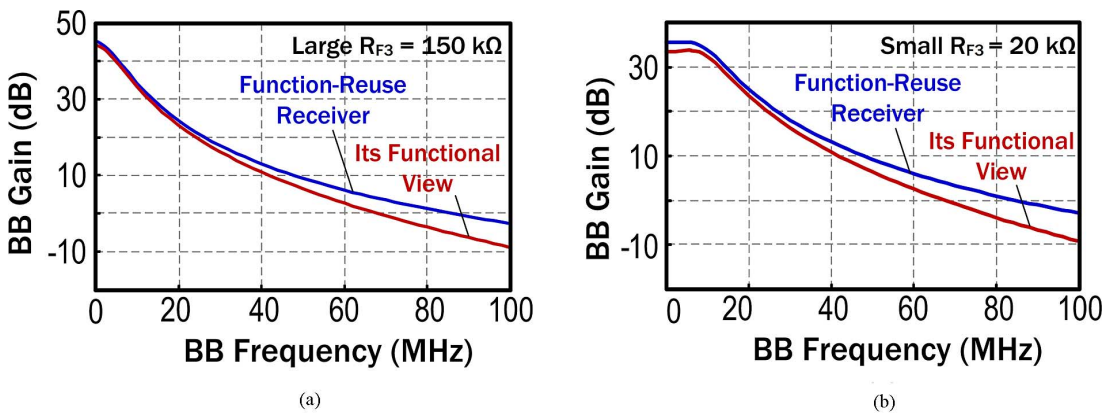

Fig. 10. Simulated BB gain response of the function-reuse receiver and its functional view with (a) a large R_{F3} and (b) a small R_{F3}.

ever, with a large R_{F3}, the RF NF for the three architectures is almost equal since they have similar RF and BB gains as shown in Fig. 12(a)–(d). From Figs. 11 and 12, it can be conclude that, although the RF gain of the function-reuse receiver has ~10 dB difference, the difference in the BB NF is small (0.2 dB). However, for the functional view model, the BB NF has about 2 dB difference. The NTF from the RF input to the LNA's output V_o can be derived similarly to [11] by LPTV analysis.

IV. Low-Voltage Current-Reuse VCO-Filter

In order to further optimize the power, the VCO is designed to current-reuse with the BB complex low-IF filter (Fig. 13). The negative transconductor of the VCO is divided into multiple M_V cells. The aim is to distribute the bias current of the VCO to all BB gain stages $(A_1, A_2 \ldots A_{18})$ that implement the BB filter. For the VCO, M_V operates at the frequency of $2f_s$ or $4f_s$ for

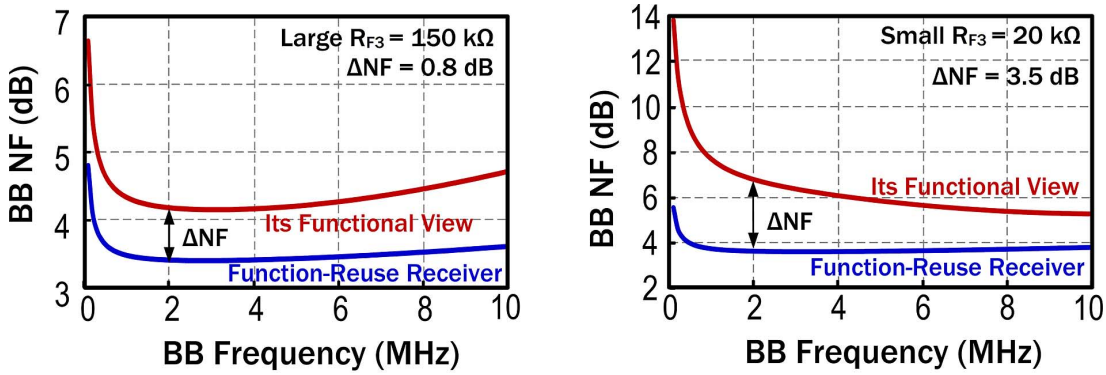

(a) (b)

Fig. 11. Simulated BB NF of the function-reuse receiver and its functional view with (a) a large R_{F3} and (b) a small R_{F3}.

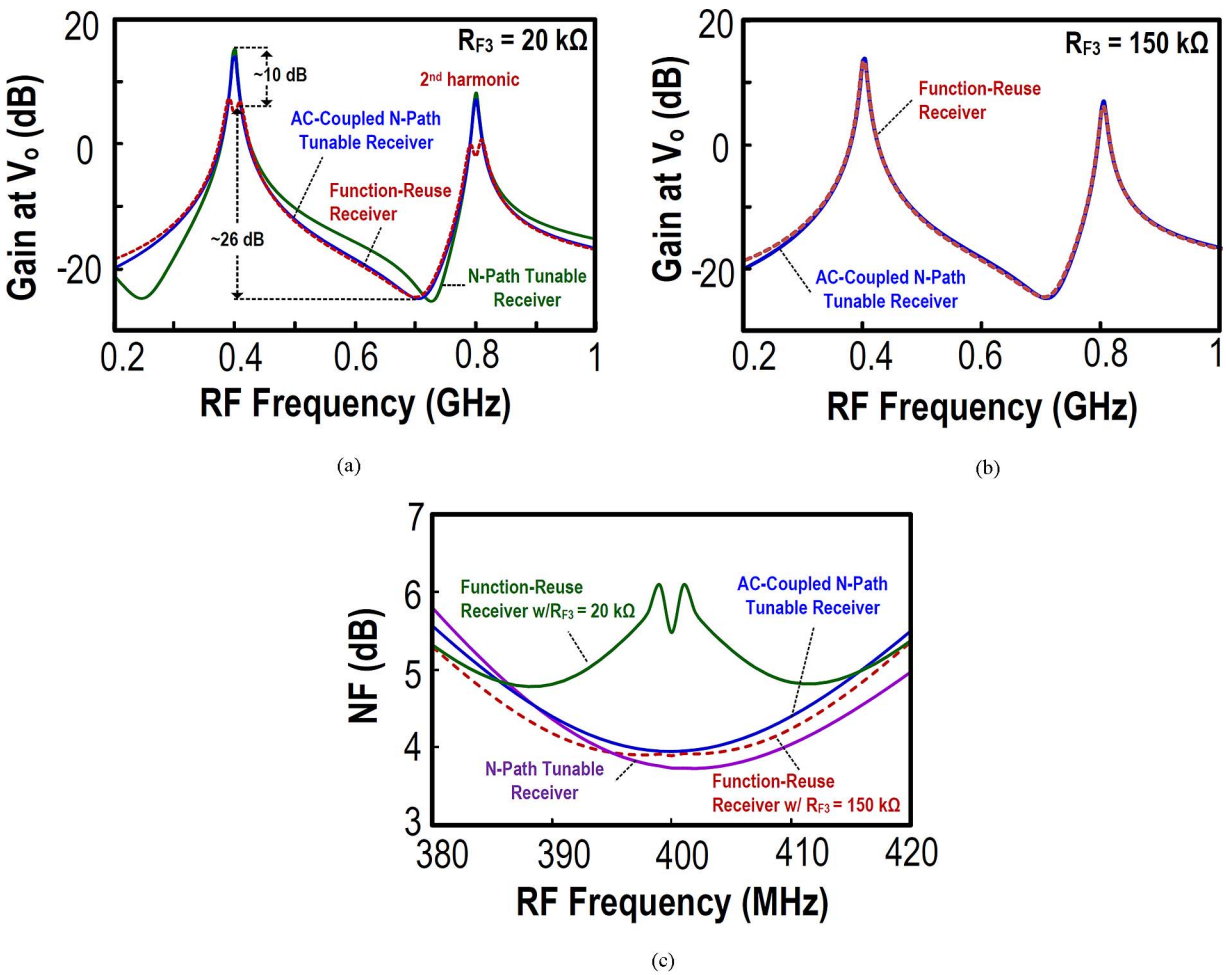

(a) (b)

(c)

Fig. 12. Simulated (a)–(b) RF gain responses at V_o and (c) RF NF at V_o for the three architectures: 4-path tunable receiver, AC-coupled 4-path tunable receiver and function-reuse receiver with a gain-boosted 4-path SC network. The simulation parameters are $R_L = 800\,\Omega, R_s = 50\,\Omega, g_{m1} = 4g_{m2} = 4g_{m3} = 20.55$ mS, $C_i = 12.5$ pF, $f_s = 400$ MHz, $R_{F1} = 5$ kΩ and $R_{F2} = 20$ kΩ.

a div-by-2 or div-by-4 circuit. Thus, the VCO signal leaked to the source nodes of $M_V(V_{F1,I+}, V_{F1,I-})$ is pushed to very high frequencies ($4f_s$ or $8f_s$) and can be easily filtered by the BB capacitors. For the filter's gain stages such as A_1, $M_b(g_{Mb})$ is loaded by an impedance of $\sim 1/2g_{Mv}$ when L_p can be considered as a short circuit at BB. Thus, A_1 has a ratio-based voltage gain of roughly g_{Mb}/g_{Mv}, or as given by $4Tg_{Mb}/G_{mT}$, where G_{mT} is the total transconductance for the VCO tank. The latter shows how the distribution factor T can enlarge the BB gain, but is a tradeoff with its input-referred noise and can add more layout parasitics to $V_{vcop,n}$ (i.e., narrower VCO's tuning range). The $-R$ cell using cross-coupled transistors is added at $V_{F1,I+}$ and $V_{F1,I-}$ to boost the BB gain without loss of voltage headroom. For the BB complex poles, $A_{2,5}$ and C_{f1} determine the

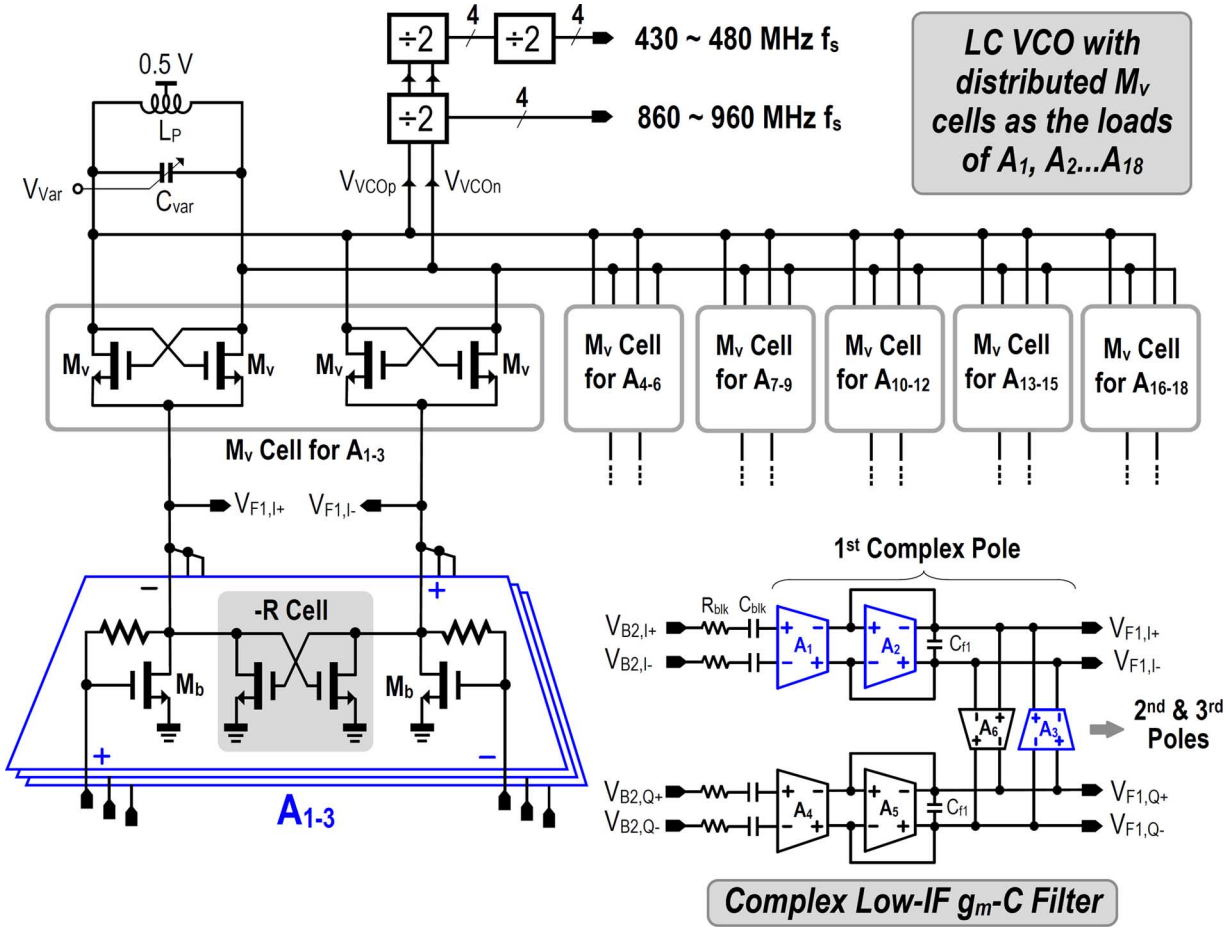

Fig. 13. Proposed low-voltage current-reuse VCO-filter.

real part while $A_{3,6}$ and C_{f1} yield the imaginary part. There are three similar stages cascaded for higher channel selectivity and image rejection ratio (IRR). R_{blk} and C_{blk} were added to avoid the large input capacitance of $A_{1,4}$ from degrading the gain of the front-end.

V. Experimental Results

Two versions of the multi-ISM-band sub-GHz ZigBee receiver were fabricated in 65 nm CMOS (Fig. 14) and optimized with a single 0.5 V supply. With (without) the LC tank for the VCO, the die area is 0.2 mm^2 (0.1 mm^2). Since the measurement results of both are similar, only those measured with VCO in Fig. 15(a)–(d) are reported here. From 433 to 960 MHz, the measured BB gain is 50 ± 2 dB. Following the linearity test profile of [20], two tones at $[f_s + 12$ MHz, $f_s + 22$ MHz$]$ are applied, measuring an OB-IIP3 of -20.5 ± 1.5 dBm at the maximum gain. The IRR is 20.5 ± 0.5 dB due to the low-Q of the VCO-filter. The IIP3 is mainly limited by the VCO-filter. The measured NF is 8.1 ± 0.6 dB. Since the VCO is current-reuse with the filter, it is interesting to study its phase noise with the BB signal amplitude. For negligible phase noise degradation, the BB signal swing should be < 60 mV_{pp}, which can be managed by variable gain control. If a 60 mV_{pp} BB signal is insufficient for demodulation, a simple gain stage (e.g., inverter amplifier) can be added after the filter to enlarge the gain and output swing. The total power of the receiver is 1.15 mW (0.3 mW for the LNA+BB amplifiers and 0.65 mW for VCO-filter and 0.2 mW for the divider), while the phase noise is -117.4 ± 1.7 dBc/Hz at 3.5 MHz frequency offset. The S_{11} is below -8 dB across the

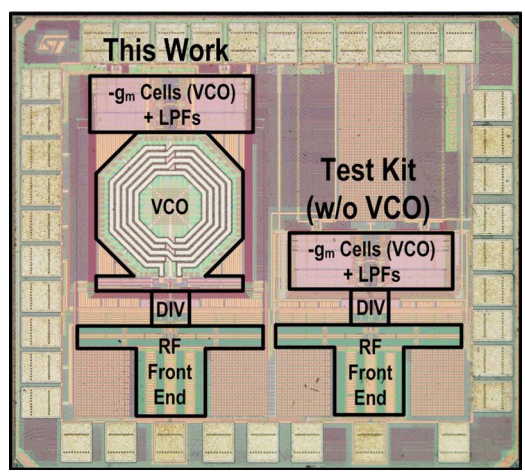

Fig. 14. Chip micrograph of the function-reuse receiver with a LC-tank for the VCO (left) and without it (right).

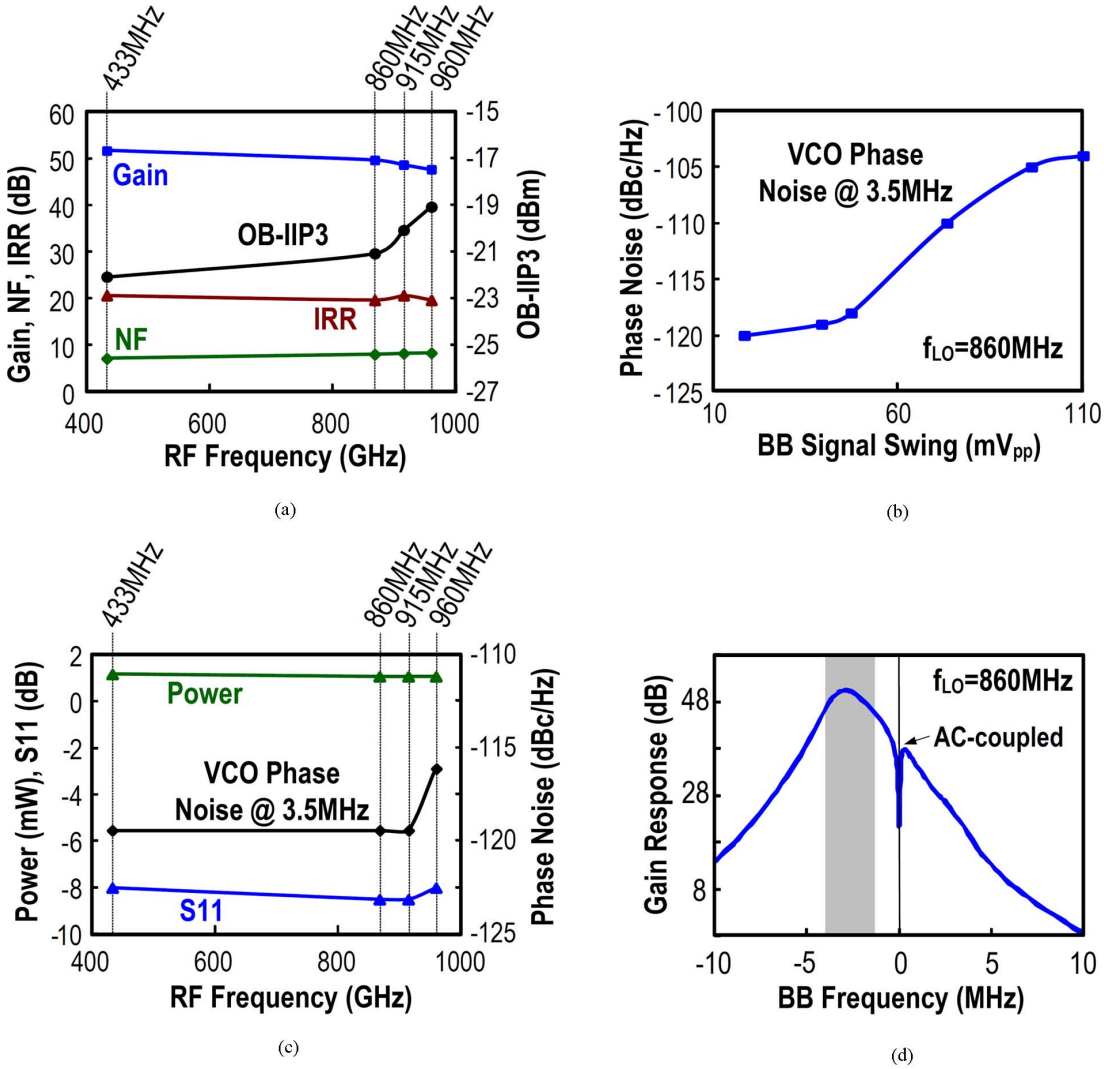

Fig. 15. Measured key performance metrics: (a) Gain, NF, IRR and OB-IIP3. (b) VCO phase noise versus BB signal swing. (c) S11, power and VCO phase @ 3.5 MHz offset. (d) BB complex gain response centered at −2 MHz IF.

whole band. The asymmetric IF response shows 24 dB (41 dB) rejection at the adjacent (alternate) channel.

To study the RF filtering behavior, the P_{1dB} and blocker NF are measured. For the in-band signal, the P_{1dB} is -55 dBm while with a frequency offset frequency of 20 MHz, it increases to -35 dBm, which is mainly due to the double-RF filtering [Fig. 16(a)]. For an offset frequency of 60 MHz, the P_{1dB} is -20 dBm, limited by the current-reuse VCO-filter. For the blocker NF, with a single tone at 50 MHz, the blocker NF is almost unchanged for the blocker <-35 dBm. With a blocker power of <-20 dBm, the NF is increased to $\sim$14 dB [Fig. 16(b)].

The chip summary and performance benchmarks are given in Table I, where [15] and [20] are current-reuse architectures while [14] is the classical cascade architecture with ULV supply for energy harvesting. For this work, the results measured under an external LO are also included for completeness. In both cases, this work succeeds in advancing the power and area efficiencies with multi-band convergence, while achieving tunable S_{11} with zero external components. Particularly, when comparing with the most recent ULV design [14], this work saves more than $10\times$ of area while supporting multi-band operation with zero external components.

VI. Conclusions

A function-reuse receiver embedding a gain-boosted N-path SC network has been proposed to realize a sub-GHz multi-ISM-band ULP ZigBee radio at a single 0.5 V supply. The featured improvements are fourfold: 1) unlike the usual receiver concept that is based on cascade of blocks, this receiver reuses one set of amplifiers for concurrent RF and BB amplification by arranging an N-path SC network in the feedback loop. Interestingly, this scheme decouples the BB STF (or NTF) from its RF STF (or NTF), allowing a lower BB NTF possible while saving power and area. This new receiver concept is good foundation for a deeper exploration of the topic. 2) The output BB NTF due to R_{sw} and R_F are greatly reduced, lowering the required size of

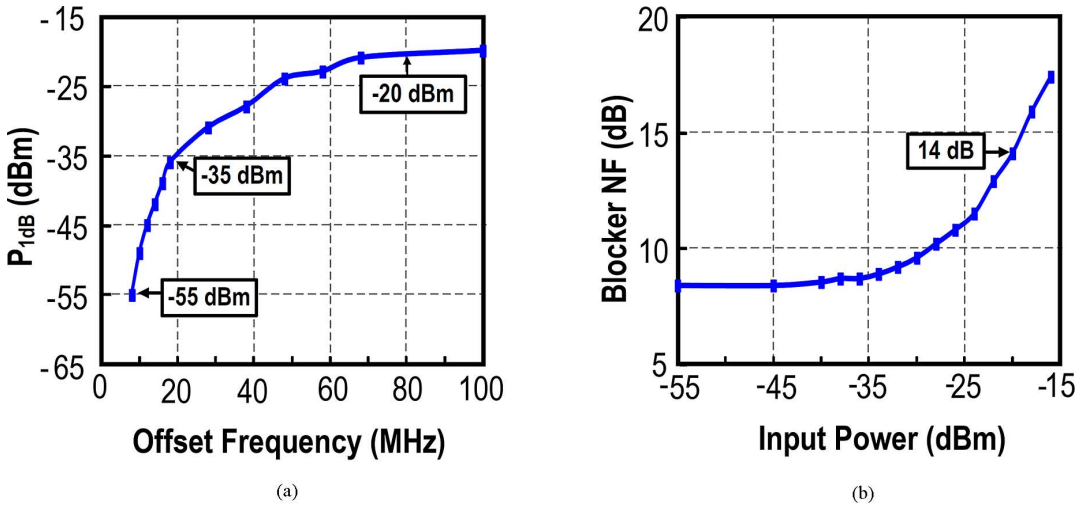

Fig. 16. Measured (a) P_{1dB} versus innput offset frequency and (b) blocker NF versus input power.

TABLE I
PERFORMANCE SUMMARY AND BENCHMARK WITH THE STATE-OF-THE-ART

	This Work	ISSCC'13 [15] (w/ VCO)	ISSCC'13 [14]	JSSC'10 [20]
Application	**433/860/915/960 MHz (ZigBee/IEEE802.15.4c/d)**	2.4 GHz (ZigBee/ IEEE 802.15.4)	2.4 GHz (Energy Harvesting)	2.4 GHz (ZigBee/ IEEE 802.15.4)
Architecture	Function-Reuse RF Front-End + N-path Tunable LNA + Current-Reuse VCO-Filter	Blixer + Hybrid Filter + Passive RC-CR Filter + LC VCO	CG LNA + Passive Mixers + N-Path SC IF Filter + LC VCO	LNA-Mixer-VCO Merged Cell + Complex Filter
BB Filter	3 complex poles	1 Biquad, 4 complex poles	2 real poles	3 complex poles
Input Matching Technique	**On-chip N-path SC (tunable by LO, high Q)**	On-chip LC (fixed, low Q)	Off-chip LC (fixed, low Q)	Off-chip LC (fixed, high Q)
External Components	**zero**	zero	2 caps, 1 inductor	1 caps, 1 inductor
Input Matching BW and Tunability	**433 to 960 MHz (tunable by LO)**	2.25 to 3.55 GHz (fixed)	~ 2 to 2.6 GHz (fixed)	2.3 to 2.6 GHz (fixed)
Active Area (mm^2)	**0.2 (*0.1)**	0.3	2.5	0.35
Power (mW) @V_{DD}	**1.15 ± 0.05 @ 0.5 V**	2.7 @ 0.6/1.2 V	1.6 @ 0.3 V	3.6 @ 1.2 V
Gain (dB)	50 ± 2 (*51 ± 3)	55	83	75
NF (dB)	8.1 ± 0.6 (*8 ± 1)	9	6.1	9
OB-IIP3 (dBm)	–20.5 ±1.5 (*–23 ± 1)	–6	–21.5	–12.5
IRR (dB)	20.5 ± 0.5 (*21 ± 0.5)	28	N/A	35
VCO Phase Noise (dBc/Hz)	–117.4 ± 1.7 @ 3.5 MHz	–115 @ 3.5 MHz	–112 @ 1 MHz	–116 @ 3.5 MHz
Technology	65 nm CMOS	65 nm CMOS	65 nm CMOS	90nm CMOS

* Results measured from the test kit that has no VCO.

the mixer switches and LO power. 3) Double-RF filtering is performed with one N-path SC network, improving the OB-IIP3 and tolerability of OB blockers. 4) A current-reuse VCO-filter further optimizes the power at just 0.5 V. All of these characteristics affirm the receiver as a potential candidate for emerging ULP radios for IoT applications that should support multi-band operation, being friendly to a single ULV supply for energy harvesting, and compact enough to save cost in nanoscale CMOS.

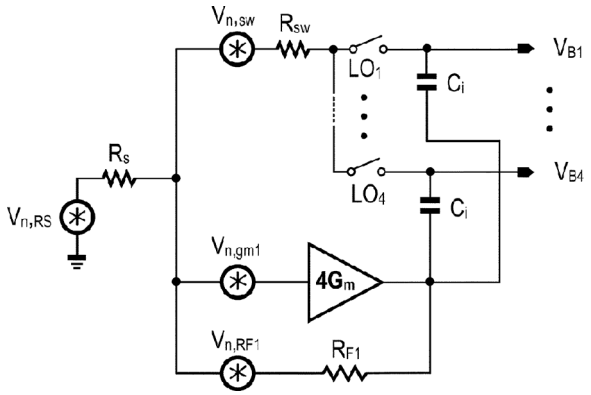

Fig. 17. Equivalent noise model of the N-path tunable receiver [Fig. 3(d)] for BB output-noise PSD calculation and simulation. $\mathrm{N} = 4$ is used. The noise sources $\mathrm{g_{m1}}$ and $\mathrm{R_{F1}}$ from the $4\mathrm{G_m}$ are explicitly shown.

APPENDIX

Output-Noise PSD at BB for the N-Path Tunable Receiver:

The derivation of the output-noise PSD at BB due to $\mathrm{R_S}$, $4\mathrm{G_m}$, $\mathrm{R_{sw}}$ and $\mathrm{R_{F1}}$ is presented here. The model used to obtain the NTFs is shown in Fig. 17. For all output-noise PSDs, there are two parts: one is the direct transfer from input RF to BB (Part A), while another is from harmonics folding noise (Part B). For the latter, increasing the path number N can reduce such contribution. The differential output-noise PSD for $\mathrm{R_s}$, $4\mathrm{G_m}$, $\mathrm{R_{sw}}$ and $\mathrm{R_{F1}}$ with $\overline{\mathrm{V^2_{n,R_S}}} = 4\mathrm{KTR_s}$, $\overline{\mathrm{V^2_{n,Gm}}} = 4\mathrm{KT/g_{m1}}$, $\overline{\mathrm{V^2_{n,Rsw}}} = 4\mathrm{KTR_{sw}}$ and $\overline{\mathrm{V^2_{n,R_{F1}}}} = 4\mathrm{KTR_{F1}}$ are given as shown in (12)–(15) at the bottom of the page. For the above NTFs, the even-order terms (including zero) of n are excluded. The single-ended HTFs for $\mathrm{R_S}$, $4\mathrm{G_m}$, $\mathrm{R_{sw}}$ and $\mathrm{R_{F1}}$ are $\mathrm{H_{n,R_S}(j\omega)}$, $\mathrm{H_{n,4Gm}(j\omega)}$, $\mathrm{H_{n,R_{sw}}(j\omega)}$ and $\mathrm{H_{n,R_{F1}}(j\omega)}$, respectively. The derivation is similar to $\mathrm{H_{n,RF}(j\omega)}$ in Section III-A. The only difference is on the linear state-space equation. Further details were covered in [11].

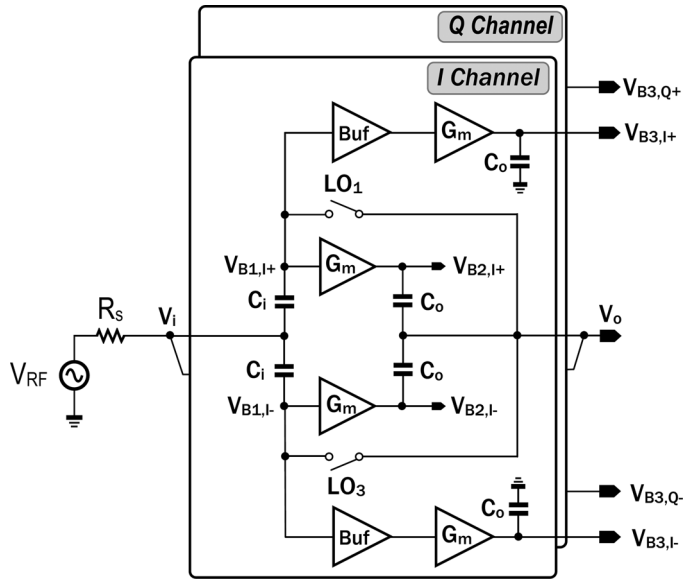

Fig. 18. Schematic to model the BB NF of the functional-reuse receiver at $\mathrm{V_{B2,I\pm}}$.

$$\overline{\mathrm{V^2_{n,out,R_S}}} = \left\{ \underbrace{\left|\mathrm{H_{-1,R_S}(j\omega)V_{n,R_S}(j\omega+\omega_s)}\right|^2}_{\text{Part A}} + \underbrace{\sum_{\mathrm{n=-\infty,n\neq-1}}^{\infty} \left|\mathrm{H_{n,R_S}(j\omega)V_{n,R_S}(j(\omega-n\omega_s))}\right|^2}_{\text{Part B}} \right\} \times 4 \tag{12}$$

$$\overline{\mathrm{V^2_{n,out,Gm}}} = \left\{ \underbrace{\left|\mathrm{H_{-1,4Gm}(j\omega)V_{n,4Gm}(j\omega+\omega_s)}\right|^2}_{\text{Part A}} + \underbrace{\sum_{\mathrm{n=-\infty,n\neq-1}}^{\infty} \left|\mathrm{H_{n,4Gm}(j\omega)V_{n,4Gm}(j(\omega-n\omega_s))}\right|^2}_{\text{Part B}} \right\} \times 4 \tag{13}$$

$$\overline{\mathrm{V^2_{n,out,R_{sw}}}} = \left\{ \underbrace{\left|\mathrm{H_{-1,R_{sw}}(j\omega)V_{n,R_{sw}}(j\omega+\omega_s)}\right|^2}_{\text{Part A}} + \underbrace{\sum_{\mathrm{n=-\infty,n\neq-1}}^{\infty} \left|\mathrm{H_{n,R_{sw}}(j\omega)V_{n,R_{sw}}(j(\omega-n\omega_s))}\right|^2}_{\text{Part B}} \right\} \times 4 \tag{14}$$

$$\overline{\mathrm{V^2_{n,out,R_{F1}}}} = \left\{ \underbrace{\left|\mathrm{H_{-1,R_{F1}}(j\omega)V_{n,R_{F1}}(j\omega+\omega_s)}\right|^2}_{\text{Part A}} + \underbrace{\sum_{\mathrm{n=-\infty,n\neq-1}}^{\infty} \left|\mathrm{H_{n,R_{F1}}(j\omega)V_{n,R_{F1}}(j(\omega-n\omega_s))}\right|^2}_{\text{Part B}} \right\} \times 4 \tag{15}$$

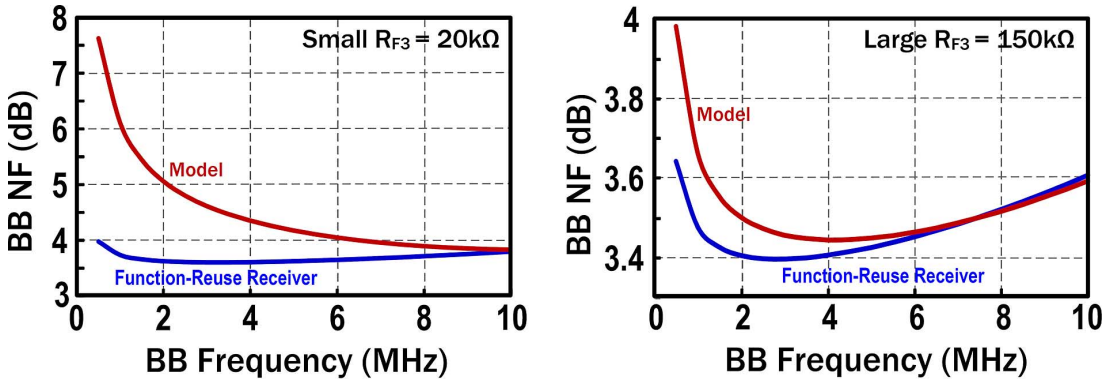

(a) (b)

Fig. 19. Simulated BB NF from the model and functional-reuse receiver with (a) a small R_{F3} and (b) a larger R_{F3}.

Derivation and Modeling of BB Gain and Output Noise for the Function-Reuse Receiver:

When considering the memory effect of the capacitor C_i and C_o with R_{F3} sufficiently large, the voltages (i.e., the circuit states) at C_i are independent [19]. In the steady-state, around the clock frequency, the voltages sampling at C_i are $v_{Ci}(t)$, $jv_{Ci}(t)$, $-v_{Ci}(t)$, $-jv_{Ci}(t)$, while the voltage sampling at C_o is $v_{CO}(t)$, $jv_{CO}(t)$, $-v_{CO}(t)$, $-jv_{CO}(t)$, for LO_{1-4}, respectively. When LO_1 is high ($K = 1$), linear analysis shows the following state-space description for capacitor C_i:

$$\begin{cases} \begin{cases} \frac{C_i dv_{Ci}(t)}{dt} = (v_{B1,I+}(t) + v_{B1,I-}(t) + v_{B1,Q+}(t) \\ \qquad +v_{B1,Q-}(t))g_{m3} \\ \quad +(v_{B2,I+}(t) + v_{B2,I-}(t) + v_{B2,Q+}(t) \\ \qquad +v_{B2,Q-}(t)) = \frac{1}{4R_L} \end{cases} \\ \frac{v_{RF}(t)-v_i(t)}{R_S} = \frac{C_i dv_{Ci}(t)}{dt} \\ v_i(t) = v_{Ci}(t) + v_o(t) + R_{sw}\frac{C_i dv_{Ci}(t)}{dt} \\ v_i(t) - v_{B1,I+}(t) = v_{Ci}(t) \\ v_i(t) - v_{B1,I-}(t) = -v_{Ci}(t) \\ v_i(t) - v_{B1,I-}(t) = -v_{Ci}(t) \\ v_i(t) - v_{B1,Q+}(t) = jv_{Ci}(t) \\ v_i(t) - v_{B1,Q-}(t) = -jv_{Ci}(t) \\ v_o(t) + v_{co}(t) = v_{B2,I+}(t) \\ v_o(t) - v_{co}(t) = v_{B2,I-}(t) \\ v_o(t) + jv_{co}(t) = v_{B2,Q+}(t) \\ v_o(t) + jv_{co}(t) = v_{B2,Q-}(t). \end{cases} \tag{16}$$

Equation (16) can be simplified similar to (1). Likewise, when LO_1 is low, it can be described by (4). Thus, it has the same BB HTFs as in gain-boosted N-path SC network [shown also in (8)].

The BB NF at $V_{B2,I\pm}(V_{B2,Q\pm})$ is approximately modeled in Fig. 18. The BB output noise at $V_{B1,I\pm}(V_{B1,Q\pm})$ are further amplified by two separate BB amplifiers, while in the function-reuse receiver they are amplified by the same BB amplifiers. From simulations, with a large R_{F3}, the model has a good accuracy, while for a small R_{F3}, the error increases for the low-frequency part. This is because the BB gain at $V_{B1,I\pm}(V_{B1,Q\pm})$ gets smaller under a small R_{F3}, and the independent noise sources from the model's G_m contribute additional noise [Fig. 19(a) and (b)]. Still, this model is more accurate than that of the functional view [Fig. 19(c)]. For both cases, the function-reuse receiver has a smaller NF and requires lower power than the separated G_m situation. For the BB gain, this model has a high accuracy (not shown).

REFERENCES

[1] J. A. Stankovic, "Research directions for the Internet of Things," *IEEE Internet of Things J.*, vol. 1, no. 1, pp. 3–9, Feb. 2014.

[2] A. Zanella, N. Bui, A. Castellani, L. Vangelista, and M. Zorzi, "Internet of things for smart cities," *IEEE Internet of Things J.*, vol. 1, no. 1, pp. 22–32, Feb. 2014.

[3] Pike Research on Smart Cities. 2Q, 2014 [Online]. Available: http://www.pikeresearch.com/research/smart-cities

[4] J. Sinderen *et al.*, "Wideband UHF ISM-band transceiver supporting multichannel reception and DSSS modulation," in *IEEE ISSCC Dig. Tech. Papers*, 2013, pp. 454–455.

[5] A. Wong *et al.*, "A 1 V 5 mA multimode IEEE 802.15.6/Bluetooth low-energy WBAN transceiver for biotelemetry applications," in *IEEE ISSCC Dig. Tech. Papers*, 2012, pp. 300–301.

[6] B. W. Cook, A. Berny, A. Molnar, S. Lanzisera, and K. Pister, "Low-power, 2.4-GHz transceiver with passive RX front-end and 400-mV supply," *IEEE J. Solid-State Circuits*, vol. 41, no. 12, pp. 2767–2775, Dec. 2006.

[7] Z. Lin, P.-I. Mak, and R. P. Martins, "A 0.14-mm^2 1.4-mW 59.4-dB-SFDR 2.4 GHz ZigBee/WPAN receiver exploiting a split-LNTA +50% LO topology in 65-nm CMOS," *IEEE Trans. Microw. Theory Tech.*, vol. 62, no. 7, pp. 1525–1534, Jul. 2014.

[8] A. Mirzaei and H. Darabi, "Analysis of imperfections on performance of 4-phase passive-mixer-based high-Q bandpass filters in SAW-less receivers," *IEEE Trans. Circuits Syst. I, Reg. Papers*, vol. 58, no. 5, pp. 879–892, May 2011.

[9] A. Ghaffari, E. Klumperink, M. Soer, and B. Nauta, "Tunable high-Q N-path band-pass filters: Modeling and verification," *IEEE J. Solid-State Circuits*, vol. 46, no. 5, pp. 998–1010, May 2011.

[10] J. Han and R. Gharpurey, "Recursive receiver down-converters with multiband feedback and gain-reuse," *IEEE J. Solid-State Circuits*, vol. 43, no. 9, pp. 1119–1131, Sep. 2008.

[11] Z. Lin, P.-I. Mak, and R. P. Martins, "Analysis and modeling of a gain-boosted N-path switched-capacitor bandpass filter," *IEEE Trans. Circuits Syst. I, Reg. Papers*, vol. 61, no. 9, pp. 2560–2568, Sep. 2014.

[12] Z. Lin, P.-I. Mak, and R. P. Martins, "A 0.5 V 1.15 mW 0.2 mm^2 sub-GHz ZigBee receiver supporting 433/860/915/960 MHz ISM bands with zero external components," in *IEEE ISSCC Dig. Tech. Papers*, 2014, pp. 164–165.

[13] F. Zhang, Y. Miyahara, and B. Otis, "Design of a 300-mV 2.4-GHz receiver using transformer-coupled techniques," *IEEE J. Solid-State Circuits*, vol. 48, no. 12, pp. 3190–3205, Dec. 2013.

[14] F. Zhang, K. Wang, J. Koo, Y. Miyahara, and B. Otis, "A 1.6 mW 300 mV supply 2.4-GHz receiver with −94 dBm sensitivity for energy-harvesting applications," in *IEEE ISSCC Dig. Tech. Papers*, 2013, pp. 456–457.

[15] Z. Lin, P.-I. Mak, and R. P. Martins, "A 1.7 mW 0.22 mm^2 2.4 GHz ZigBee RX exploiting a current-reuse Blixer + hybrid filter toploly in 65 nm CMOS," in *IEEE ISSCC Dig. Tech. Papers*, 2013, pp. 448–449.
[16] Z. Lin, P.-I. Mak, and R. P. Martins, "A 2.4-GHz ZigBee receiver exploiting an RF-to-BB-current-reuse Blixer + hybrid filter topology in 65-nm CMOS," *IEEE J. Solid-State Circuits*, vol. 49, no. 6, pp. 1333–1344, Jun. 2014.
[17] C. Andrews and A. Molnar, "Implications of passive mixer transparency for impedance matching and noise figure in passive mixer-first receivers," *IEEE Trans. Circuits Syst. I, Reg. Papers*, vol. 57, no. 12, pp. 3092–3103, Dec. 2010.
[18] C. Andrews and A. Molnar, "A passive mixer-first receiver with digitally controlled and widely tunable RF interface," *IEEE J. Solid-State Circuits*, vol. 45, no. 12, pp. 2696–2708, Dec. 2010.
[19] M. Soer, E. Klumperink, P. d. Boer, F. v. Vliet, and B. Nauta, "Unified frequency domain analysis of switched-series-RC passive mixers and samplers," *IEEE Trans. Circuits Syst. I, Reg. Papers*, vol. 57, no. 10, pp. 2618–2631, Oct. 2010.
[20] M. Tedeschi, A. Liscidini, and R. Castello, "Low-power quadrature receivers for ZigBee (IEEE 802.15.4) applications," *IEEE J. Solid-State Circuits*, vol. 45, no. 9, pp. 1710–1719, Sep. 2010.

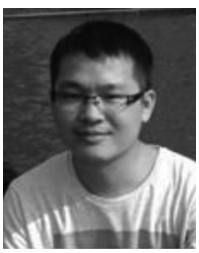

Zhicheng Lin received the B.S. and the M.S. degrees in physics from Lanzhou University and South China Normal University, China, in 2005 and 2009, respectively. He is currently working towards the Ph.D. degree at the State Key Laboratory of Analog and Mixed-Signal VLSI and FST-ECE, University of Macau, Macau, China.

His current research focuses on ULP radio front-ends and the RF circuit techniques for wideband software-defined radio front-ends.

Pui-In Mak (S'00–M'08–SM'11) received the Ph.D. degree from the University of Macau (UM), Macao SAR, China, in 2006.

He is currently an Associate Professor at UM and Coordinator of the Wireless and Biomedical Research Lines of the State Key Laboratory of Analog and Mixed-Signal VLSI. His research interests are in analog and RF circuits and systems for wireless, biomedical and physical chemistry applications. His group has reported six state-of-the-art chips at ISSCC: wideband receivers (2011, 2014), micro-power amplifiers (2012, 2014) and ultra-low-power ZigBee receivers (2013, 2014), and pioneered the world's first Intelligent Digital Microfluidic Technology (iDMF) with nuclear magnetic resonance (NMR) and polymerase chain reaction (PCR) capabilities. He has authored two books: *Analog-Baseband Architectures and Circuits for Multistandard and Low-Voltage Wireless Transceivers* (Springer, 2007), and *High-/Mixed-Voltage Analog and RF Circuit Techniques for Nanoscale CMOS* (Springer, 2012).

His involvements with IEEE are: Distinguished Lecturer (2014–2015) and Member of Board of Governors (2009–2011) of IEEE Circuits and Systems Society (CASS); Editorial Board Member of IEEE Press (2014–2016); Senior Editor of IEEE JOURNAL ON EMERGING AND SELECTED TOPICS IN CIRCUITS AND SYSTEMS (2014–2015); Associate Editor of IEEE TRANSACTIONS ON CIRCUITS AND SYSTEMS I (TCAS-I) (2010–2011, 2014); Associate Editor of IEEE TRANSACTIONS ON CIRCUITS AND SYSTEMS II (TCAS-II) (2010–2013), and Guest Editor of IEEE RFIC VIRTUAL JOURNAL (2014) for the issue on LNA. He has been a TPC member of A-SSCC since 2013.

Prof. Mak received the IEEE DAC/ISSCC Student Paper Award 2005, the IEEE CASS Outstanding Young Author Award 2010, the National Scientific and Technological Progress Award 2011, and the Best Associate Editor for TCAS-II 2012–2013. In 2005, he was decorated with the Honorary Title of Value for scientific merits by the Macau Government.

Rui P. Martins (M'88–SM'99–F'08) was born on April 30, 1957. He received the Bachelor (5 years), Masters, and Ph.D. degrees, as well as the *Habilitation* for Full Professor in electrical engineering and computers from the Department of Electrical and Computer Engineering, Instituto Superior Técnico (IST), TU of Lisbon, Portugal, in 1980, 1985, 1992, and 2001, respectively.

He has been with the Department of Electrical and Computer Engineering (DECE)/IST, TU of Lisbon, since October 1980. Since 1992, he has been on leave from IST, TU of Lisbon, and is with the Department of Electrical and Computer Engineering, Faculty of Science and Technology (FST), University of Macau (UM), Macao, China, where he has been a Full Professor since 1998. In FST he was the Dean of the Faculty from 1994 to 1997 and he has been Vice Rector of the University of Macau since 1997. From September 2008, after the reform of the UM Charter, he was nominated after open international recruitment as Vice Rector (Research) until August 31, 2013. Within the scope of his teaching and research activities, he has taught 21 bachelor and master courses and has supervised (or co-supervised) 26 theses, Ph.D. (11) and Masters (15). He has published 12 books, co-authoring five and co-editing seven, plus five book chapters, 266 refereed papers in scientific journals (60) and in conference proceedings (206), as well as 70 other academic works, for a total of 348 publications. He has also co-authored seven U.S. patents. He created the Analog and Mixed-Signal VLSI Research Laboratory of UM: http://www.fst.umac.mo/en/lab/ans_vlsi/website/index.html, elevated in January 2011 to State Key Lab of China (the First in Engineering in Macao), being its Founding Director.

Prof. Martins was the Founding Chairman of the IEEE Macau Section from 2003 to 2005, and of the IEEE Macau Joint Chapter on Circuits And Systems (CAS)/Communications (COM) from 2005 to 2008 [2009 World Chapter of the Year of the IEEE Circuits And Systems Society (CASS)]. He was the General Chair of the 2008 IEEE Asia-Pacific Conference on Circuits and Systems—APCCAS'2008, and was the Vice President for Region 10 (Asia, Australia, and the Pacific) of the IEEE Circuits and Systems Society (CASS), for 2009–2011. He was also the Vice President (World) Regional Activities and Membership of the IEEE CAS Society for 2012–2013. He is an Associate Editor of the IEEE TRANSACTIONS ON CIRCUITS AND SYSTEMS II: EXPRESS BRIEFS for 2010–2013. He is a member of the IEEE CASS Fellow Evaluation Committee (Class of 2013). He was the recipient of two government decorations: the Medal of Professional Merit from Macao Government (Portuguese Administration) in 1999, and the Honorary Title of Value from Macao SAR Government (Chinese Administration) in 2001. In July 2010, he was elected unanimously as Corresponding Member of the Portuguese Academy of Sciences (in Lisbon), being the only Portuguese Academician living in Asia.